



HAL
open science

Novel multi-feature bar design for machine tools geometric errors identification

Fabien Viprey, Hichem Nouira, Sylvain Lavernhe, Christophe Tournier

► To cite this version:

Fabien Viprey, Hichem Nouira, Sylvain Lavernhe, Christophe Tournier. Novel multi-feature bar design for machine tools geometric errors identification. *Precision Engineering*, 2016, 46, pp.323-338. 10.1016/j.precisioneng.2016.06.002 . hal-01357513

HAL Id: hal-01357513

<https://hal.science/hal-01357513>

Submitted on 1 Sep 2016

HAL is a multi-disciplinary open access archive for the deposit and dissemination of scientific research documents, whether they are published or not. The documents may come from teaching and research institutions in France or abroad, or from public or private research centers.

L'archive ouverte pluridisciplinaire **HAL**, est destinée au dépôt et à la diffusion de documents scientifiques de niveau recherche, publiés ou non, émanant des établissements d'enseignement et de recherche français ou étrangers, des laboratoires publics ou privés.

Novel multi-feature bar design for machine tools geometric errors identification

F.VIPREY^{a,b,*}, H.NOUIRA^a, S.LAVERNHE^b, C.TOURNIER^b

^aLaboratoire Commun de Métrologie (LNE-CNAM), Laboratoire National de Métrologie et d'Essais (LNE)
1, rue Gaston Boissier, 75724 PARIS Cedex 15, France

^bLURPA, ENS Cachan, Univ. Paris-Sud, Université Paris-Saclay, 94235 Cachan, France

Abstract

This paper describes the development of a new thermo-invariant material standard (new Multi-Feature Bar (MFB) standard) and an associated procedure for the identification of 21 geometric errors on 3-axis machine tools (MT). The design of the new standard allows to extract 3 intrinsic parameters for each position of the MFB: 1 linear positioning error and 2 straightness errors.

To ensure the metrology traceability chain to the SI metre definition, the calibration of the MFB is carried out using an accurate traceable coordinate measuring machine (CMM) when applying the reversal technique. The established procedure for the identification of the geometric errors was applied on a 5-axis MT, leading to the identification of the apparent 21 geometric errors of the 3 linear axes. To achieve with this purpose, the number of required positions of the MFB was optimized and reduced to only 6 positions, while using both rotary axes. The collection of raw data for each measurement was performed thanks to an accurate touch probe, linear encoders of the MT, as well as a developed interface that is independent of the industrial computer numerical control (CNC). Furthermore, the sensitivity of the geometric errors on the linear axes position are highlighted.

Keywords: New material standard, Reversal technique, Calibration, Geometric errors, Machine tools

1. Introduction

With the progress in technology, the demand of high accurate parts becomes a classical need in industry. The manufacture of these parts is usually performed via high precision machine tools (MT) traceable [1] to the SI metre definition published at the intergovernmental organization "Bureau International des Poids et Mesures (BIPM)". Hence, the traceability of MTs represents a new challenge for several researchers involved in National Metrology Institutes (NMIs) and/or in manufacturing laboratories or plants. Some of them investigate the calibration of MTs using physical standards previously calibrated on high precision coordinate measuring machine (CMM) [2]. Such way of MTs calibration can be carried out on line. Others researchers extend the calibration process to inspect produced parts under the manufacturing process, directly in the MTs. Several sources of errors in MTs can be identified in the literature (e. g. thermal, geometrical, resolution, vibration) with the geometrical error being the most important one: it can be estimated to more than 70% of the entire error [3].

Several standards and procedures for the calibration of MTs are detailed in ISO 230-1:2012 [4] and ISO 230-7:2007 [5] and include: gauge blocks, step gauges, ball bars, hole bars, ball plates, hole plates, straightedges, microscopes, taut wire, laser angle interferometer, autocollimator, precision level and digital scale.

Cauchick-Miguel et al. [6] describe the most important standards and suggest a classification of various testing methods for mechanical material standards. Moreover, Knapp et al. [7] distinguished and compared different common material standards regarding selected criteria. Some of them are the certification, length of standard, reversal method, transportability, handling, cleaning, ability to detect geometric errors and especially the number of positions for checking all errors.

The following review and analysis of the common standards and devices for the calibration of CMM and MT justifies the development of a new material standard.

1.1. Gauge blocks

Gauge blocks are usually made with steel or ceramic materials and used to check the geometric errors of CMM [7, 8]. Osawa et al. [9] used a gauge block to compensate the CMM

*Corresponding author

Email address: fabien.viprey@ens-cachan.fr (F.VIPREY)

geometric errors when calibrating a cylinder by applying the substitution or reversal techniques. The use of gauge blocks requires at least 21 positions and different lengths to identify 21 geometric errors, which represent a high number of operations to perform a MT calibration.

1.2. Step gauges

The step gauges offer the possibility to identify only one intrinsic parameter (linear positioning error). They are well used for testing the CMM calibration, as well as for correcting the error components ascertained by the calibration procedure. The calibration test procedure is defined in the ISO 10360-2:2009 [8], such as 5 calibrated test lengths should be considered for the 7 specified positions (locations and orientations). 4 of the 7 positions shall be the space diagonals.

Busch et al. [10] used a step gauge to check the CMM calibration in 2 diagonals of the workspace, while Pahk and Kim [11] used a step gauge to identify the linear positioning errors of a CMM. Such type of standard is not frequently used in MT since the calibration procedure can be considered as too long.

1.3. Ball bars and hole bars

Ball bar is a common material standard used to identify the geometric errors in both MTs and CMMs [12], and exists in various types.

In particular, the Fixed Magnetic Ball Bar (FMBB) is well used to identify the geometric errors by measuring the distance between 2 datum spheres at least in 20 positions in the CMM workspace [13]. Nevertheless, the Telescopic Magnetic Ball Bar (TMBB) was developed especially for the identification of the geometric errors of MT. By combining several measurements with multi-axes motions, both position and orientation axes errors of a MT were identified [14]. A triangular ball bar was developed and used by Jouy and Clément [15] in several positions to identify the angular errors and squareness errors for both CMM and MT. An additional improved architecture of the ball bar was proposed by Zhang and Zang [16] to identify the 21 geometric errors in CMM and MT. Its architecture is based on several equispaced datum spheres (made with steel materials) linearly fixed on a rigid beam via steel rods.

The calibration procedure of the latter architecture was defined by Ouyang and Jawahir [17], while it was based on two indirect comparisons of measurements performed in two positions. An accurate calibration of the ball bar was carried out on a precision CMM, where the motion errors were compensated via several substitution measurements using a gauge block. Currently, ceramic material is frequently selected for the datum spheres, where the form errors can reach a sub-micrometre level [2].

Another type of material standard is the hole bar, which is used for the identification of the 21 geometric errors of CMM [18]. This type of material standard can provide only two intrinsic parameters: one positioning error and one straightness. Thus, at least 17 positions of the hole bar are necessary to determine the whole 21 geometric errors.

For MT calibration, the use of ball bar seems to be more suitable than the hole bar due to the accessibility of features.

Tilted orientations of the ball bar can be measured by the touch probe, even if its axis is not perfectly collinear with the spheres rods. This configuration is unrealisable with the hole bar. However, the use of the ball bar can present many disadvantages such as: risk of collisions with the datum spheres, thermal drift of the rods, the risk of a crash of the spheres surfaces, highly sensitive to harsh environment. The ball bar calibration by reversal technique is nearly impossible, which can drastically influence its accuracy.

1.4. Ball plates and Hole plates

At NPL (United Kingdom NMI), a ball plate was developed for the verification of the performance of coordinate measurement systems and particularly CMM softwares [19]. It is made of steel material. At PTB (Germany NMI), the Zerodur hole plate was also developed to identify the 21 geometric errors of CMMs [20, 21] that can be directly obtained by calculating the residual between the measured and calibrated positions of the holes. This operation requires once only four positions of the hole plate in the CMM workspace: two horizontal and two vertical positions. An accurate calibration of the Hole plate is performed by applying the reversal technique.

However, the main disadvantage of the hole plate used on MT is linked to its orientation with regards to the probing device. Thus, if both the hole plate and the spindle supporting the probing system are aligned in the same axis, the measurement of the hole plate becomes difficult. This limitation significantly reduces the use of hole plate, even if it provides the identification of 6 geometric errors for each selected position.

To come up with the discussed limitation, a set of a ball plate and spacers was developed by Liebrich et al. [22] and calibrated on CMM. Afterwards, it was used for the calibration of a 3-axis MT [23]. Since the spindle supporting the probing system was oriented vertically, the ball plate was located in the horizontal position. The volumetric calibration (3D mesh) of the MT was performed using the set of the spacers at different heights. Based on the analysis of the ball plate design, interdependency between the angular errors (roll, pitch and yaw) can be observed, but this issue was minimized thanks to the proposed mathematical procedure. Furthermore, the design of the ball plate is highly sensitive to the clamping system, which can generate significant mechanical deformations. The deformations directly impact the local positions of the datum spheres supposed to be fixed. The centre of the datum spheres can change to reach some micrometres thereby representing a supplementary issue of the ball plate standard use. In addition, the proposed design of the ball plate is highly sensitive to the surrounding thermal drift in the manufacturing shop floor.

1.5. Supplementary material standard

Some material standards similar to a space frame was developed and calibrated on a traceable CMM [24, 25]. They were used only for a checking operation of the volumetric machine geometry and not for the identification of the geometric errors. Based on the checking results, the re-calibration of the geometric errors of the machine should be performed only for the

coordinates where the errors exceed the maximal permissible error (MPE) [8].

Choi et al. [26] developed a cube array artefact with 8 cubes to determine the geometric model parameters necessary for the mapping of the tool's positioning error. The straightness errors can be deduced by considering both the angular errors and the squarenesses.

Another technique was developed for 5-axis MTs by Mayer [27]. This technique was based on the use of several uncalibrated master balls fixed on the rotary table. The use of this technique enables the identification of both the position and the orientation axes errors, as well as some additional motion errors of a 5-axis MT.

To identify the geometric errors of a MT, some other techniques were proposed by Ibaraki et al. [28] and Pezeshki et al. [29], where they applied a machining test, succeeded by CMM measurements performed on the manufactured workpieces. A comparison between the measurement data and the CAD model leads to identify the geometric errors. However, the identification results seem to be affected by the thermal errors, spindle errors, cutting forces, vibrations, and environment conditions.

1.6. Laser interferometer systems

The laser system is a common system typically used for the calibration of MTs [30]. It requests an adjustment step that consists in the alignment of the laser beam along the MT axis equipped with an optical artefact. This first step can be time consuming. A recent compact Laser Tracer system based on the multilateration principle was developed by Schwenke [31]. It ensures lower uncertainty than the laser tracker [32]. All these laser systems are directly traceable to the SI meter definition. The wavelength is sensitive to the temperature, humidity and pressure, which can be measured and compensated when applying the updated formula of Birch and Downs [33]. Such systems are also highly sensitive to harsh environment and vibration. Moreover, the setting system (tripod, floor) can lengthen the metrology loop and can influence the measurement results.

1.7. Conclusion on the existing material standards

Most of the existing material standards are developed for CMM calibration, except the ball plates, 1D-ball array, and TMBB. Hence, the touch probe clamped in the spindle axis of the MT represents the main limitation to use most of them. Moreover, the harsh environment (oil, chips, collisions, temperature drift, etc.) also reduces their integration in MTs. Some aforementioned material standards require too many positioning configurations to identify the 21 geometric errors of 3 linear axes structural loop. Thus, any automation of the calibration process becomes very complex since it requires several adjustments, and usually the calibration is handled manually. In addition, steel and ceramic material are commonly selected for these standards. Because these materials are sensitive to the variation of the surrounding temperature, they are non-adapted for interim MT checking or calibration during the production process in the manufacturing shop floor.

A new design of the Multi-Feature Bar (MFB) is proposed in this paper. thanks to its new geometric pattern, it allows to identify 1 linear positioning error and 2 straightnesses of any linear mechanical guiding system of the MT, and just by 1 measurement of the MFB. The identification of 3 parameters for one orientation of the MFB leads to minimize MT's downtime. Furthermore, the combination of measurements performed on two parallel positions of the MFB leads to maximized the number of identified geometric errors to 5 (1 linear positioning error, 2 straightnesses and 2 angular errors for each axis).

This paper is organized as detailed below. Section 2 presents the design and technical attributes of the new thermo-invariant MFB standard that will be used for dimensional metrology on MTs dimensional measurements under harsh shop floor environmental conditions. The section 3 deals with the calibration of the proposed MFB by applying reversal technique. The calibration results are presented and discussed in section 4, while the section 5 is devoted to the identification of geometric errors of an investigated MT. Finally, section 6 details identification results and discussions.

2. New design of the thermo-invariant MFB standard

2.1. Concept of the thermo-invariant MFB

The new design of the MFB consists in a repetition of a 3D pattern in one direction. Each pattern contains 7 features: 4 flat surfaces (vertical planes) and 3 cylinders (one vertical inner cylinder and two horizontal outer cylinders). The patterns are repeated along the direction Δ as illustrated in (Figure 1a), where $1 \leq i \leq N$ and $1 \leq j \leq N - 1$. Many measurements are carried out on each pattern. The processing of the measured data allows to extract one point corresponding to the intersection of the 7 features mentioned previously. The expected measurements and the post-processing of the measured data can be completed with respect to the following steps:

- at least 8 points should be measured on each hole HOL_i with a touch probe, as shown in Figure 1b. They are distributed in 2 orthogonal sections (2 levels): 4 equispaced points in the upper-level and the others in the lower-level. According to ISO5459:2011 [34], the extraction is achieved by association to define the associated feature and performed with the measured dataset. A nominal cylinder is associated to the 8 measured points by applying the least squares criteria, based on small displacement screw (SDS) method [35]. The least squares SDS method for cylinder is detailed in Appendix A. Thereafter, the intrinsic characteristics of each associated feature establishing the common datum shall be considered to determine the $AXIS_i$ as shown in Figure 1b;
- at least 4 points should be measured on each flat surfaces PL with a touch probe, as shown in Figure 1c. Based on the ISO 5459:2011 [34], the post-processing of the measured dataset with the least squares plane association allows to define the associated integral feature (nominal

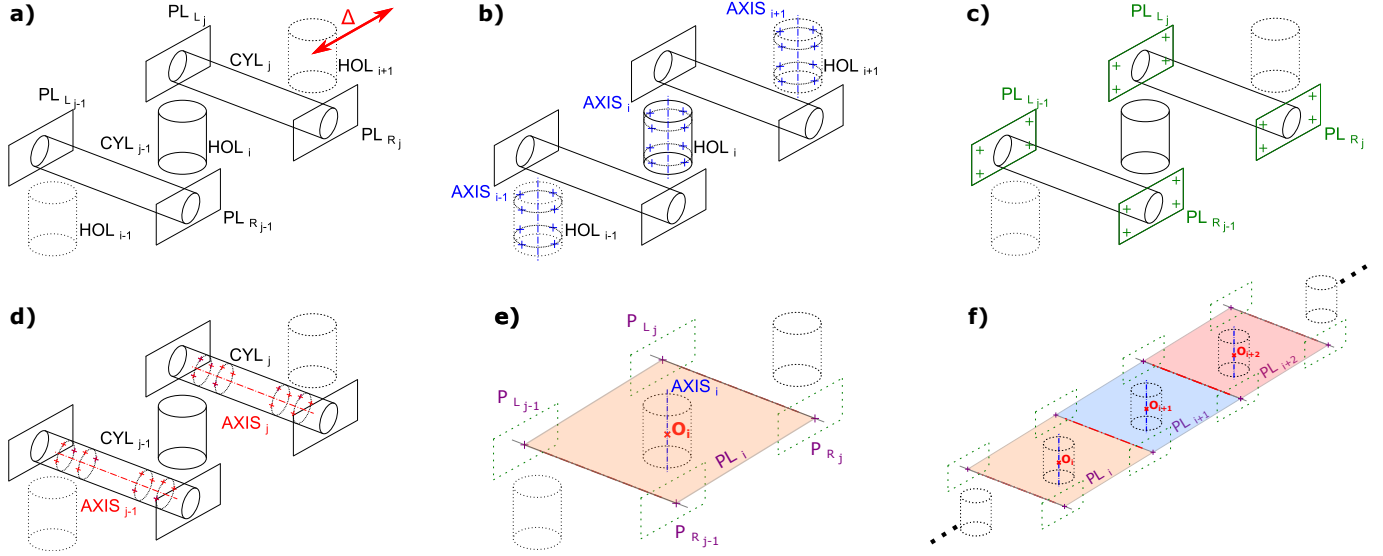


Figure 1. Principle of MFB: Patterns, probed points, and points of interest.

plane PL_{L_j} or PL_{R_j}). The association method is detailed in Appendix B;

- for each horizontal outer cylinder CYL_j , 12 points shall be probed as shown in Figure 1d. The points are distributed in 4 orthogonal sections where 3 equispaced points should be measured for each section. The analysis of the measured data using the developed SDS method allows to determine $AXIS_j$;
- the points P_{L_j} and P_{R_j} are obtained mathematically and correspond to the intersection of $AXIS_j$ with both planes PL_{L_j} and PL_{R_j} as illustrated in Figure 1e. The horizontal least squares plane PL_i is associated to the 4 points $P_{L_{j-1}}$, $P_{R_{j-1}}$, P_{L_j} and P_{R_j} . The last step consists in the identification of the point of interest O_i that corresponds to the intersection of $AXIS_i$ and PL_i ;

The previously detailed steps are repeated as many times to cover the whole geometry of the MFB (Figure 1f). Thus, the identified points of interest $O_i = (x_i, y_i, z_i)$ offer 3 intrinsic geometric parameters in the local frame of the MFB : 1 linear positioning and 2 straightnesses. R_{MFB} is built using the measured data on the different surfaces constituting the patterns as follows:

- a least squares plane PL_{ref} is associated to the 4 points P_{L_1} , P_{R_1} , $P_{L_{N-1}}$ and $P_{R_{N-1}}$ (in Figure 2) leading to the identification of the \vec{z}_{MFB} axis, which corresponds to the outer-pointing normal of PL_{ref} ;
- the intersections between PL_{ref} and $AXIS_1$ as well as PL_{ref} and $AXIS_N$ are the points O_1 and O_N that are used for the \vec{x}_{MFB} identification (normalized vector $\overrightarrow{O_1O_N}$);
- the \vec{y}_{MFB} is the cross product $\vec{z}_{MFB} \wedge \vec{x}_{MFB}$.

As a consequence, R_{MFB} is equal to $(O_1, (\vec{x}_{MFB}, \vec{y}_{MFB}, \vec{z}_{MFB}))$ when exploiting both horizontal $AXIS_1$ and $AXIS_{N-1}$. Nevertheless, the building of R_{MFB} can be performed using any two $AXIS_j$ ($1 \leq j \leq N - 1$) and any two O_i ($1 \leq i \leq N$).

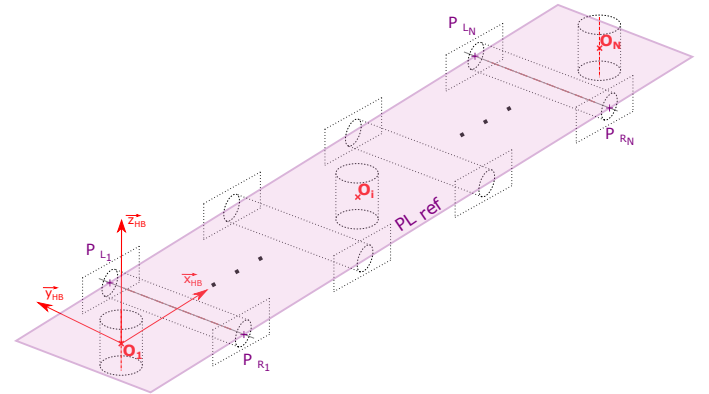


Figure 2. Definition of local frame R_{MFB} of the MFB.

2.2. Technical and geometrical attributes of the MFB

The MFB is expected to be used for on line measurement, directly on the MT under severe conditions (coolant, lubricant, chips, risks of collisions and temperature gradient). Based on the NF E 11 019 [36], technical and geometrical attributes were considered such as:

- the material combines a small coefficient of thermal expansion (CTE), a high toughness and small brittleness. The Invar material seems the best candidate material compared to those presented in table 2.2 and has been therefore selected due to its small CTE, its high toughness and its small brittleness as shown in table 2.2. Its CTE is

twenty times larger than CTE of Zerodur but remains extremely low. For the chosen dimensional characteristics of the MFB, the deviation between two points of interest is only $0.5 \mu\text{m}$ under a temperature gradient of 10°C ;

- all the patterns are accessible via two sides (above or below). This condition is useful for repositioning the MFB in relation to the ball bar (i.e. rigid beam with several equispaced datum spheres) during the calibration when applying the reversal separation error technique. Besides, the application of the reversal technique on the MT enables the identification of the motion errors of each linear axis;
- the surfaces to be measured are protected against any possible collision due to their position. All of the holes were manufactured using a wire electrical discharge machining (WEDM). The rods were machined and carefully ground (Figure 4);
- two selected holes axes were shifted with respect to the nominal \vec{x}_{MFB} axis, in order to identify the orientation (returned or not returned) of the MFB whatever of its positioning in the workspace of the MT. Therefore, the MFB is provided of mistake-proofing which ensures the physical signature of the MFB;
- the MFB is fixed on a specific holder, built with modular inspection equipment system, via isostatic assembly composed of 3 mechanical linkages (spherical joint, point surface joint and point curve joint). This type of assembly avoids a transmission of the mechanical and thermal deformation of the holder to the MFB. The 3 mechanical linkages are located on the points of minimum deflection that were analytically calculated and are not exactly identical to Airy points. The points of minimum deflection are separated by a length $s_{min\ def}$ defined by the equation 1 where $L = 580 \text{ mm}$. However, between the Airy points, the length s_{Airy} is defined by the equation 2. As illustrated in figure 3, this precaution minimizes the deflection of the MFB under its own weight ($0.16 \mu\text{m}$ without tightening operation). This value is compensated by reversal technique during the calibration of MFB.

$$s_{min\ def} = 0.5537 \times L = 321.1 \text{ mm} \quad (1)$$

$$s_{Airy\ points} = \frac{1}{\sqrt{3}}L = 334.9 \text{ mm} \quad (2)$$

Moreover, modular inspection equipment system allows to orientate and locate the MFB along each direction in the MT workspace (Figure 5). The change in length of the MFB when standing vertically, due to its own weight, is equal to 52 nm and is neglected with respect to the magnitude of the identified errors ($0 - 100 \mu\text{m}$).

To characterize a maximum volume of the selected Mikron 5axis MT workspace, the developed and manufactured MFB has been defined as follows: the $N-1 = 11$ rods ($AXIS_j$) and the $N = 12$ holes ($AXIS_i$) are equispaced ($L = 50 \text{ mm}$) along the \vec{x}_{MFB} axis.

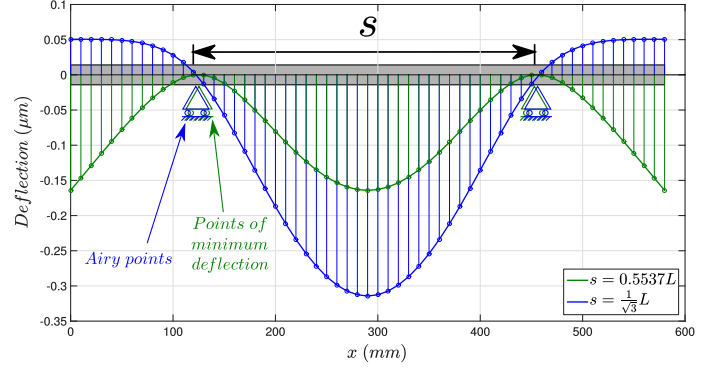


Figure 3. Deflection of a bar under its own weight.

Table 1. Mechanical properties of Zerodur, Invar, Al_2O_3 and S235 materials.

Material	CTE (α) $\mu\text{m}/^\circ\text{C}/\text{m}$	Young's modulus (E) GPa	Hardness (H) MPa	Toughness (Kc) $\text{MPa}\cdot\text{m}^{1/2}$	Brittleness (H/Kc) $\text{m}^{-1/2}$
Zerodur	0.05	91	6200	0.9	6900
Invar	1	145	1200	120	10
Al_2O_3	8	350	20000	4	5000
S235	12	210	1000	50	20

3. Calibration of the MFB

The nominal coordinates of points of interest (O_i) in the local frame R_{MFB} are defined in equation 3. Nevertheless, the real coordinates of the points (O_i) are slightly different from these expressed in the proposed model. This difference is mainly caused by the manufacturing procedure of the MFB including the Computer-Aided Manufacturing (CAM), interpolation, WEDM accuracy, material removal process, etc. Thus, a thorough calibration of the MFB has to be performed to extract the intrinsic geometric errors: one linear positioning error ($E_{xx_{MFB}}$) and two straightnesses ($E_{yx_{MFB}}$, and $E_{zx_{MFB}}$). Therefore, the realistic model of the MFB can be written as equation 4.

$$\forall i \in \llbracket 1 ; N \rrbracket, \begin{pmatrix} x_i \\ y_i \\ z_i \end{pmatrix}_{R_{MFB}} = \begin{pmatrix} (i-1) \times L \\ 0 \\ 0 \end{pmatrix}_{R_{MFB}} \quad (3)$$

$$\forall i \in \llbracket 1 ; N \rrbracket, \begin{pmatrix} x_i \\ y_i \\ z_i \end{pmatrix}_{R_{MFB}} = \begin{pmatrix} (i-1) \times L & + E_{xx_{MFB}}(i) \\ 0 & + E_{yx_{MFB}}(i) \\ 0 & + E_{zx_{MFB}}(i) \end{pmatrix}_{R_{MFB}} \quad (4)$$

For the calibration of the MFB, the reversal technique ([4, 9, 16, 37]) is applied in order to separate the motion errors of the used accurate CMM from the geometric errors of the MFB. This technique concerns only the straightnesses and never the positioning errors. Thus, the absolute length between each hole can be corrected by a substitution technique [9, 17].

The motion errors of a CMM contain both systematic component (E_{CMM}) and random component (ϵ_{CMM}). The application of the reversal technique enables to determine the systematic

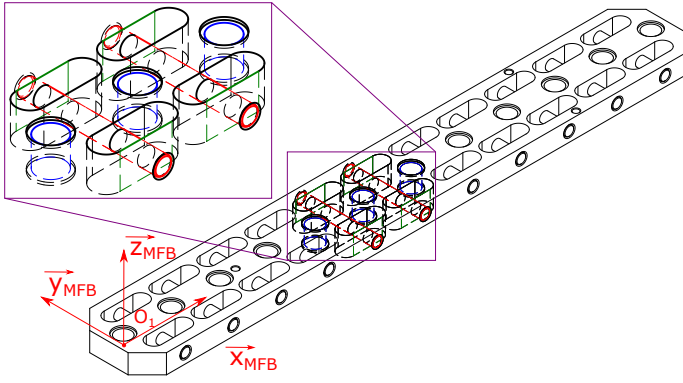


Figure 4. 3D-CAD model of MFB.

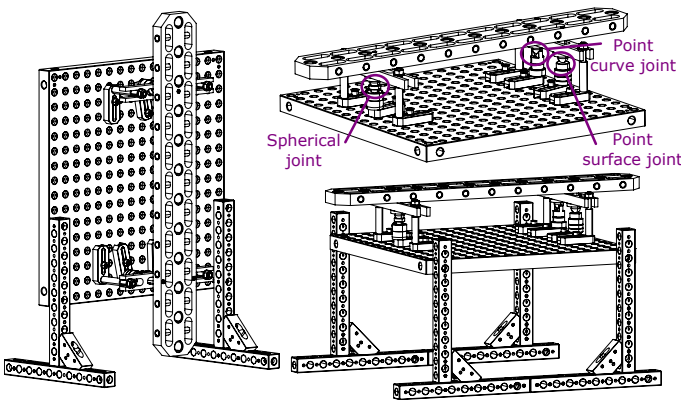


Figure 5. MFB holder: vertical and horizontal configurations.

components. The random component is still mixed with the geometric errors of the MFB, that is why the measurements are repeated many times to average out the random effects. For the application of the reversal technique, the MFB is carefully aligned along the CMM axis (X-axis in figure 6) with the smallest linear positioning error that was identified using a step-gauge ($U_{step\ gauge\ (k=2)} = 0.3\ \mu m + 1.5\ 10^{-6}L$) calibrated by a laser interferometre system traceable to the SI metre definition.

The reversal technique is illustrated in figure 6, where M_X , M_Y , M_Z are the component of measurement in the direction X, Y, and Z of R_{CMM} . $E_{y_{xMFB}}$, and $E_{z_{xMFB}}$ are the straightnesses of the MFB in the direction of y and z in R_{MFB} . Moreover, the superscripts *NR* and *R* refer to the position of the MFB: “No Reversal” or “Reversal”.

Whatever the considered straightness of the MFB, E_{MFB}^{NR} is equal to $-E_{MFB}^R$ in the machine coordinate system. According to the figure 7, the relations between the measurement and the straightnesses of the CMM and the MFB, before and after reversal, can be expressed by the equation 5. The term ϵ_{YXCMM} depicts the zero mean random error of the CMM in the direction Y along X-axis.

$$\begin{cases} E_{y_{xMFB}}(i) = M_Y^{NR}(i) + E_{YXCMM}(i) + \epsilon_{YXCMM}(i) \\ -E_{y_{xMFB}}(i) = M_Y^R(i) + E_{YXCMM}(i) + \epsilon_{YXCMM}(i) \end{cases} \quad (5)$$

Thus, the geometric errors can be calculated with respect to the equation 6.

$$\begin{cases} E_{y_{xMFB}}(i) = \frac{1}{2} [M_Y^{NR}(i) - M_Y^R(i)] + \epsilon_{YXCMM}(i) \\ E_{z_{xMFB}}(i) = \frac{1}{2} [M_Z^{NR}(i) - M_Z^R(i)] + \epsilon_{ZXCMM}(i) \end{cases} \quad (6)$$

The zero mean random error ϵ_{YXCMM} and ϵ_{ZXCMM} cannot be subtracted directly because they are algebraic values, but averaging over repeated measurements will average the random terms to close to zero if enough repetitions are used. This strategy is carried out during the calibration procedure.

Afterwards, the linear positioning error E_{xxMFB} of the MFB is calculated by using the equation 7. The linear positioning error E_{XXCMM} of the CMM is compensated by the mean of measurements before and after reversal performed along the selected axis.

$$E_{xxMFB}(i) = \frac{1}{2} [M_X^{NR}(i) + M_X^R(i)] - (i-1) \times L + E_{XXCMM}(i) + \epsilon_{XXCMM}(i) \quad (7)$$

As the zero mean random error ϵ_{YXCMM} and ϵ_{ZXCMM} , ϵ_{XXCMM} cannot be subtracted directly because they are algebraic values, but averaging over repeated measurements will average the random terms to close to zero.

The calibration procedure can be carried out directly in the MT, except for the positioning E_{xxMFB} . The application of the reversal technique allows to separate the systematic motion errors of each target axis from the straightnesses of the MFB.

The analysis of the metrology loops when calibrating the MFB with both the CMM and the MT reveals that the CMM metrology loop is much more optimized than the MT one. Since the metrology loop directly influences the measurement accuracy, the calibration of the MFB is initially performed using the CMM to enable a subsequent MT calibration. This strategy leads to minimizing each of the number of setting-up and the MT downtime.

4. Calibration results and discussions

The calibration of the MFB was performed using the LNE CMM, traceable to the SI unit metre definition, along the Z-axis (figure 8). This Z-axis was selected since it presents the smallest linear positioning errors. Calibration procedure is repeated 5 times, the duration of each of them being about 1 hour.

The obtained results of the 3 intrinsic calibrated parameters E_{xxMFB} , $E_{y_{xMFB}}$, $E_{z_{xMFB}}$ of the MFB are presented in Figures 9 and 10, respectively for the linear positioning error and the two straightnesses.

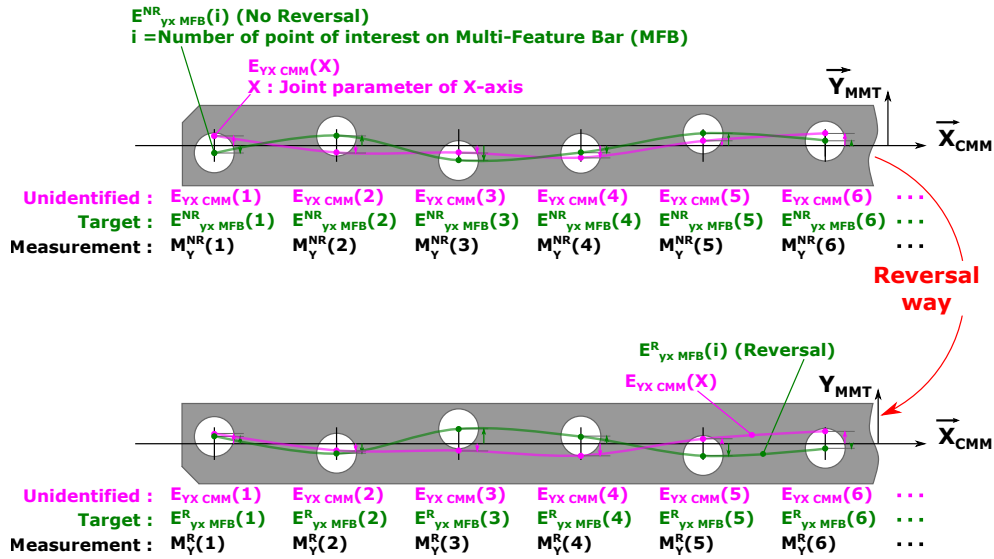


Figure 6. Reversal technique for straightness error E_{YX} of MFB aligned along X-axis of CMM.

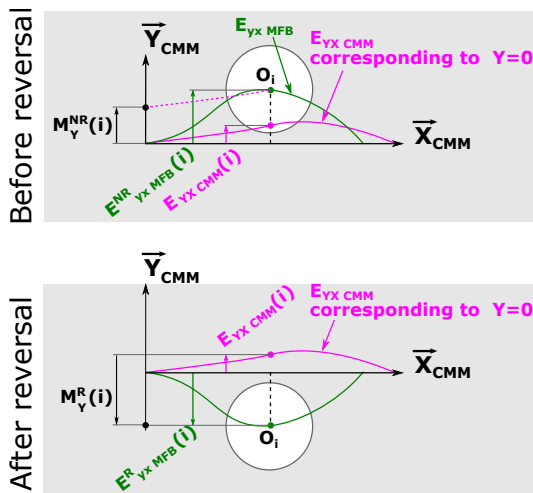


Figure 7. Reversal technique - Zoom on a point of interest O_i of the MFB.



Figure 8. MFB calibration set-up on CMM at LNE.

To obtain the results displayed in figures 9 and 10, some precautions were taken into account; in particular the mistake-proofing intentionally introduced in the design of the MFB (material standard signature) not appear in the figures. The plotted measurement uncertainty includes scatterings due to the random components of the motion errors, resolution of the probing system, environment conditions, vibrations, thermal variations and clamping system.

In figure 9, the linear positioning error of the MFB can reach a maximal value of $-42 \mu\text{m}$, which reflects the geometric error of the WEDM machine. Besides, the straightnesses reflect both the geometry errors of the WEDM machine and the assembly of the different horizontal rods carefully glued on the main frame of the MFB. The average uncertainty obtained for the linear positioning errors and straightnesses is $0.4 \mu\text{m}$ and $0.7 \mu\text{m}$ respectively, which can be considered as low values.

Based on these results, the MFB can be considered as a highly relevant thermo-invariant material standard for both CMMs or MTs calibrations.

5. Identification of geometric errors of MTs

5.1. Mikron UCP710 5-axis MT and measurement device

The calibrated MFB by reversal technique was used to map the geometric errors of the 3 linear axes of the Mikron UCP710 5-axis MT (figure 11). Hence, a high-accuracy 3D touch probe trigger was integrated in the Mikron MT. A specific interface was developed to collect, in real time, raw data provided by the 3D probe trigger as well as the linear and rotary encoders of the Mikron MT. An additional procedure was also developed to acquire the machine zero point by counting distance-coded reference marks. The developed interface is used instead of the

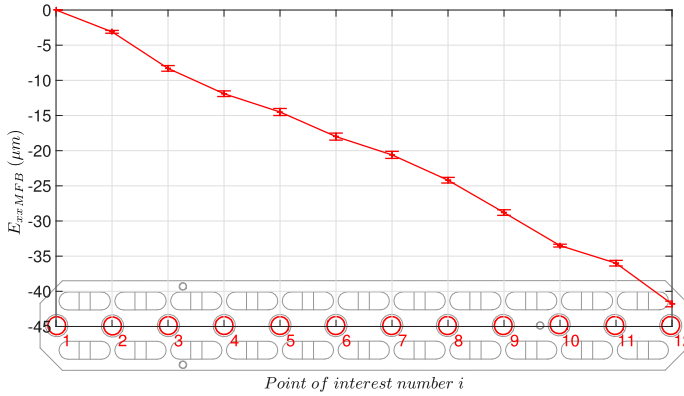


Figure 9. Linear positioning error $E_{xx_{MFB}}$ of each point of interest O_i of the MFB.

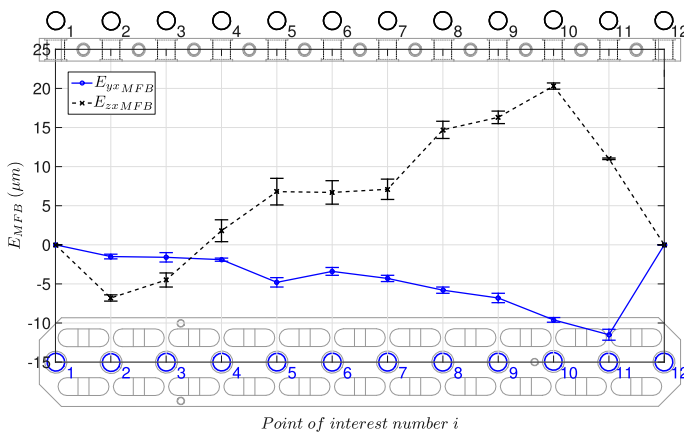


Figure 10. Horizontal straightness error $E_{yx_{MFB}}$ and vertical straightness error $E_{zx_{MFB}}$ of each point of interest O_i of the MFB.

industrial computer numerical control (CNC) of the Mikron MT to avoid collecting data with any pre-existing error compensations and uncontrolled processing. The interface ensures the measurement procedure with regards to the following steps:

1. acquisition of the MT zero point,
2. collection of the absolute MT coordinate (X, Y, Z, A, C) in real time ($f = 33 \text{ kHz}$, resolution = 10 nm) and directly on linear and rotary encoders,
3. collection of the touch probe trigger ($U_{(k=2)} = 0.25 \text{ }\mu\text{m}$ with a feedrate equal to $240 \text{ mm}\cdot\text{min}^{-1}$),
4. records of the data,
5. fetch recorded data on the hardware device.

All the data are recorded only when the touch probe trigger is activated.

5.2. Geometric model for the Mikron MT errors

A parametric model with 21 independent components was developed in order to describe the geometric errors of the 3 linear axes as defined in the ISO 230-1:2012 [4]. This parametric

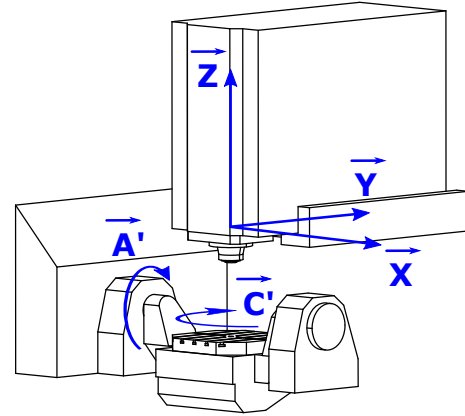


Figure 11. Mikron UCP710 5-axis machine tool structure according to the ISO 841:2004 [38] and the ISO 10791-6:2014 [39].

model was applied on the Mikron MT structural loop, considered as a rigid-body (Figure 11). The study does not include A- and C- rotary axes, but it includes the 3 linear axes X, Y and Z-axis. The 3 reference straight lines associated with 3 linear axes are defined by position and orientation errors illustrated in figure 12. According to ISO 230-1:2012 [4], errors of the zero position of linear axes (e.g. E_{X0X}) can be set to zero (0) when checking geometric accuracy of a machine tool. Moreover, as suggested in [4], the X-axis is chosen as the primary axis. Thus, the reference straight line of the X-axis coincides with the X-axis of the machine tool coordinate system (E_{B0X} and E_{C0X} can be set to zero). In the same way, the Y-axis is chosen as the secondary axis, the reference straight line of the Y-axis defines the orientation of the Y-axis of the machine tool coordinate system (E_{A0Y} can be set to zero).

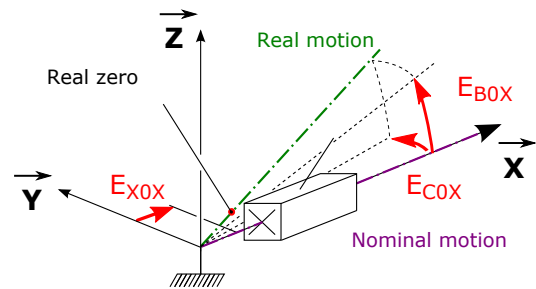


Figure 12. Location and orientation errors of reference straight line for a linear X-axis [4].

Then, each linear axis of the structural loop is composed of 2 solids constituting a link with one degree of freedom biased by geometric errors, called motion errors. According to ISO 230-1:2012 [4], 6 motion errors (Figure 13) which depend on the motion (X, Y or Z) are defined as:

- one linear positioning error along the direction of motion: $E_{XX}(X)$ along X-axis, $E_{YY}(Y)$ along Y-axis, $E_{ZZ}(Z)$ along Z-axis.
- 2 straightness errors in two orthogonal directions of mo-

tion: $E_{YX}(X)$ and $E_{ZX}(X)$ along X-axis in the direction Y and Z respectively; $E_{XY}(Y)$ and $E_{ZY}(Y)$ along Y-axis in the direction X and Z respectively; $E_{XZ}(Z)$ and $E_{YZ}(Z)$ along Z-axis in the direction X and Y respectively.

- 3 angular motion errors (i.e. roll, pitch and yaw in the case of horizontal axis): $E_{AX}(X)$, $E_{BX}(X)$ and $E_{CX}(X)$ along X-axis in the direction X, Y and Z respectively; $E_{AY}(Y)$, $E_{BY}(Y)$ and $E_{CY}(Y)$ along Y-axis in the direction X, Y and Z respectively; $E_{AZ}(Z)$, $E_{BZ}(Z)$ and $E_{CZ}(Z)$ along Z-axis in the direction X, Y and Z respectively.

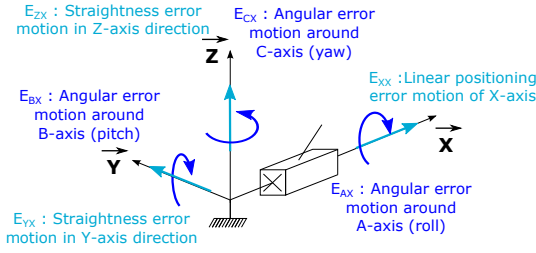


Figure 13. Motion errors for a linear X-axis [4].

To characterise the biased geometry in the structural loop, a based homogeneous transformation matrix model was investigated as in equation 8.

$$\begin{aligned}
 & \begin{bmatrix} 1 & 0 & 0 & 0 \\ 0 & 1 & 0 & 0 \\ 0 & 0 & 1 & 0 \\ 0 & 0 & 0 & 1 \end{bmatrix} \begin{bmatrix} 1 & 0 & 0 & X_{true} \\ 0 & 1 & 0 & 0 \\ 0 & 0 & 1 & 0 \\ 0 & 0 & 0 & 1 \end{bmatrix} \begin{bmatrix} 1 & -E_{CX}(X) & E_{BX}(X) & E_{XX}(X) \\ E_{CX}(X) & 1 & -E_{AX}(X) & E_{YX}(X) \\ -E_{BX}(X) & E_{AX}(X) & 1 & E_{ZX}(X) \\ 0 & 0 & 0 & 1 \end{bmatrix} \times \\
 & \begin{bmatrix} 1 & -E_{C0Y} & 0 & 0 \\ E_{C0Y} & 1 & 0 & 0 \\ 0 & 0 & 1 & 0 \\ 0 & 0 & 0 & 1 \end{bmatrix} \begin{bmatrix} 1 & 0 & 0 & 0 \\ 0 & 1 & 0 & Y_{true} \\ 0 & 0 & 1 & 0 \\ 0 & 0 & 0 & 1 \end{bmatrix} \times \\
 & \begin{bmatrix} 1 & -E_{CY}(Y) & E_{BY}(Y) & E_{XY}(Y) \\ E_{CY}(Y) & 1 & -E_{AY}(Y) & E_{YY}(Y) \\ -E_{BY}(Y) & E_{AY}(Y) & 1 & E_{ZY}(Y) \\ 0 & 0 & 0 & 1 \end{bmatrix} \times \\
 & \begin{bmatrix} 1 & 0 & E_{B0Z} & 0 \\ 0 & 1 & -E_{A0Z} & 0 \\ -E_{B0Z} & E_{A0Z} & 1 & 0 \\ 0 & 0 & 0 & 1 \end{bmatrix} \begin{bmatrix} 1 & 0 & 0 & 0 \\ 0 & 1 & 0 & 0 \\ 0 & 0 & 1 & Z_{true} \\ 0 & 0 & 0 & 1 \end{bmatrix} \times \\
 & \begin{bmatrix} 1 & -E_{CZ}(Z) & E_{BZ}(Z) & E_{XZ}(Z) \\ E_{CZ}(Z) & 1 & -E_{AZ}(Z) & E_{YZ}(Z) \\ -E_{BZ}(Z) & E_{AZ}(Z) & 1 & E_{ZZ}(Z) \\ 0 & 0 & 0 & 1 \end{bmatrix} \begin{bmatrix} 1 & 0 & 0 & -J_X \\ 0 & 1 & 0 & -J_Y \\ 0 & 0 & 1 & -J_Z \\ 0 & 0 & 0 & 1 \end{bmatrix} \begin{bmatrix} 0 \\ 0 \\ 0 \\ 1 \end{bmatrix} = \\
 & \begin{bmatrix} R_f \mathbb{R}_{R_w} & p_x \\ 0 & 0 & 0 & 1 \end{bmatrix} \begin{bmatrix} x \\ y \\ z \\ 1 \end{bmatrix}
 \end{aligned} \tag{8}$$

$$\text{where } R_f \mathbb{R}_{R_w} = \begin{bmatrix} a & d & g \\ b & e & h \\ c & f & i \end{bmatrix}$$

Where X, Y and Z are the joint parameters and J_X , J_Y and J_Z are the tool offset components. The R_{nom} frames are the nominal frames of each axis, where position and orientation errors are defined. The R_{mean} frames correspond to the mean frames attached on the reference straight line [4], where the linear motion is defined. And finally, the R_{motion} frames are the frames where motion errors are defined just after the linear motion. The workpiece positioning is defined by its orientation in the workspace R_f with the rotation matrix $R_f \mathbb{R}_{R_w}$ whose direction cosines are a, b, \dots, h, i ; while its position is defined by the vector $R_f \mathbf{p}_w = [p_x \ p_y \ p_z \ 1]^T$. The stylus centre point coordinate in R_T is $R_T \mathbf{p}_t = [0 \ 0 \ 0 \ 1]^T$. Assuming the joint parameter vector $[X \ Y \ Z]^T$ and the workpiece positioning parameters are known, the vector $R_w \mathbf{p}_w = [x \ y \ z \ 1]^T$ can be expressed as the coordinate of the probe centre point in the workpiece frame R_w which correspond to R_{MFB} .

5.3. Identification of the geometric errors using the MFB

The measurement of the patterns constituting the MFB was performed by the measurement device (touch probe) integrated in the Mikron MT. Afterwards, the points of interest O_i were extracted using the validated robust algorithms. The next step consists in the application of the developed model to identify the geometric errors of the Mikron MT.

The targeted nominal values X, Y, Z are expressed in equation 9 and correspond to the equation 8 where all geometric errors are considered equal to zero.

$$\begin{aligned}
 & \begin{bmatrix} 1 & 0 & 0 & X \\ 0 & 1 & 0 & 0 \\ 0 & 0 & 1 & 0 \\ 0 & 0 & 0 & 1 \end{bmatrix} \begin{bmatrix} 1 & 0 & 0 & 0 \\ 0 & 1 & 0 & Y \\ 0 & 0 & 1 & Z \\ 0 & 0 & 0 & 1 \end{bmatrix} \begin{bmatrix} 1 & 0 & 0 & 0 \\ 0 & 1 & 0 & 0 \\ 0 & 0 & 1 & Z \\ 0 & 0 & 0 & 1 \end{bmatrix} \begin{bmatrix} 1 & 0 & 0 & -J_X \\ 0 & 1 & 0 & -J_Y \\ 0 & 0 & 1 & -J_Z \\ 0 & 0 & 0 & 1 \end{bmatrix} \begin{bmatrix} 0 \\ 0 \\ 0 \\ 1 \end{bmatrix} = \\
 & \begin{bmatrix} R_f \mathbb{R}_{R_w} & p_x \\ 0 & 0 & 0 & 1 \end{bmatrix} \begin{bmatrix} x \\ y \\ z \\ 1 \end{bmatrix}
 \end{aligned} \tag{9}$$

The true values X_{true} , Y_{true} , Z_{true} (equation 8) are slightly different from the nominal ones due to geometric errors. From the same workpiece positioning in the workspace ($R_f \mathbb{T}_{R_w}$), and the same tool offsets, the deviation between X_{true} , Y_{true} , Z_{true} and X, Y, Z values can be evaluated by subtraction of two expressions (equation 8 and 9) and neglecting the second and higher order errors. The deviation can be stated by 3 explicit theoretical functions δ_X , δ_Y and δ_Z (equations 10, 11, 12) including several parameters such as the geometric errors, workpiece positioning, workpiece coordinate (coordinate of probe centre point expressed in R_{MFB}) and tool offsets.

$$\begin{aligned}
\delta X = X_{true} - X = & -E_{XX}(X) - E_{XY}(Y) - E_{XZ}(Z) \\
& - (E_{B0Z} + E_{BX}(X) + E_{BY}(Y)) \times G(x, y, z) \\
& + (E_{C0Y} + E_{CX}(X)) \times F(x, y, z) \\
& + E_{BZ}(Z) \times J_Z \\
& - (E_{CY}(Y) + E_{CZ}(Z)) \times J_Y
\end{aligned} \quad (10)$$

$$\begin{aligned}
\delta Y = Y_{true} - Y = & -E_{YX}(X) - E_{YY}(Y) - E_{YZ}(Z) \\
& + (E_{A0Z} + E_{AX}(X) + E_{AY}(Y)) \times G(x, y, z) \\
& - E_{AZ}(Z) \times J_Z \\
& + (E_{C0Y} + E_{CX}(X) + E_{CY}(Y) + E_{CZ}(Z)) \times J_X
\end{aligned} \quad (11)$$

$$\begin{aligned}
\delta Z = Z_{true} - Z = & -E_{ZX}(X) - E_{ZY}(Y) - E_{ZZ}(Z) \\
& - E_{AX}(X) \times F(x, y, z) \\
& + (E_{A0Z} + E_{AY}(Y) + E_{AZ}(Z)) \times J_Y \\
& - (E_{B0Z} + E_{BX}(X) + E_{BY}(Y) + E_{BZ}(Z)) \times J_X
\end{aligned} \quad (12)$$

$$\text{where } \begin{cases} F(x, y, z) = p_y + bx + ey + hz \\ G(x, y, z) = p_z + cx + fy + iz \end{cases}$$

The equations are expressed in the MT coordinate system and not in the tool centre point (TCP) in tool/probe coordinate system [18]. Furthermore, they highlight the effect of geometric errors and offsets (i.e. workpiece positioning offset and tool offset) on the measured deviation of each linear positioning-axis. From the equations (10, 11, 12), we can deduce the whole geometric errors including the linear positioning errors, straightnesses, angular errors and squarinesses.

Several measurements were performed on the thermo-invariant MFB located at wisely-selected positions such as to minimize the Abbe errors that can influence the translational motion errors (i.e. linear positioning errors and straightnesses). Afterwards, the measured data were evaluated in order to extract the points of interest (O_i), leading to obtaining the measured deviations δX , δY and δZ . The combination of numerous positions of the MFB in the workspace allows us to identify the Mikron UCP710 MT geometric errors (Figure 14). A video clip of measurement can be watched in the [Youtube page of Automated Production Research Laboratory](#). The identification procedure is sequenced as follows:

1. identification of angular motion errors using differential straightness measurements or differential linear positioning measurements,
2. identification of translational motion errors,
3. identification of squareness errors by two crossed measurements.

6. MT identification results and discussions

On 3-axis MT, 14 positions of the MFB are necessary for the identification of the apparent geometric errors (\mathbf{E}), while only 6 positions are required for 5-axis MT. The number of positions reduced to 6 for 5-axis MT is explained by the opportunity to rotate the MFB using both the swiveling axis (A' -axis according to ISO 10791-6:2014 [39]) and rotary table (C' -axis [39]), offering then several orientations of the MFB in the MT workspace. Such operation becomes possible thanks to the developed specific workholder combining several modular inspection equipment system.

Regardless of the type of selected MT and even if the number of positions is reduced, the number of the MFB measurements remains equal to 17. Each measurement spends about 14 minutes to probe 316 points covering the whole patterns. Thus, the identification of the apparent geometric errors (\mathbf{E}) can be evaluated in 1 day, including adjustments, measurements, acquisitions and data exploitation.

For the case of the Mikron UCP 710, the geometric errors of the X- Y- and Z-axis were identified, but only the results obtained with X-axis are presented in figures 15, 16 and 17. The identification of the apparent straightnesses (figure 16) is performed from the end-point reference straight line. The straight line connects the first and the last points of the measured straightness deviations [4]. In all figures, the error bars represent the uncertainty components evaluated when considering:

- measurement reproducibility including the resolution of the measuring device, the repeatability of touch probe, the random motion error of each MT-axis, vibration, thermal drift,
- position and orientation errors of the MFB in the MT-workspace,
- offset components errors of the touch probe,
- traceability chain of the MFB including the calibration process, the application of the reversal technique, the clamping system and CMM traceability,
- metrology loop including all the components that can influence the measurement. For the case of the studied Mikron MT, the metrology loop passes through the MFB (w), the 5 axes ($C'A'bXYZ$), the spindle (C1), and the touch probe (t), which can be considered as a long chain [wC'A'bXYZ(C1)t].

The measurements of the defined points for the different positions of the MFB were performed under the environment conditions (temperature between 19 and 22°C in the manufacturing shop-floor). The results for the X-axis are presented in figures 15, 16 and 17, where the markers represent the apparent error motions (E_{XX} , E_{YX} , E_{ZX} , E_{AX} , E_{BX} and E_{CX}) along the X-axis identified on the points of interest O_i ($1 \leq i \leq N$).

The apparent linear positioning error E_{XX} along the X-axis (figure 15) is rather linear and can reach a maximum value of 38 μm .

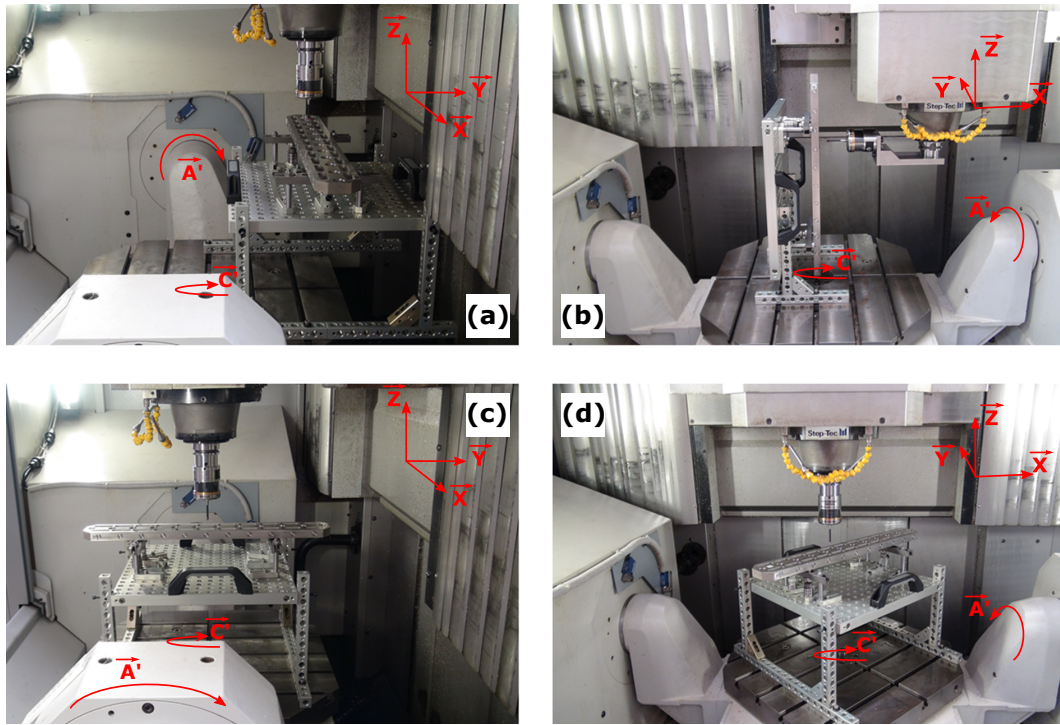


Figure 14. Calibration of the Mikron UCP710 MT using the thermo-invariant MFB: (a) along the X-axis, (b) along the Y-axis, (c) along the Z-axis, (d) along the XY plane diagonal.

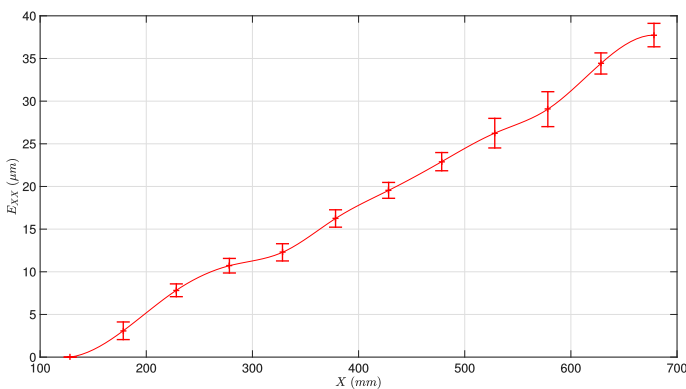


Figure 15. Linear positioning error of X-axis: E_{XX}

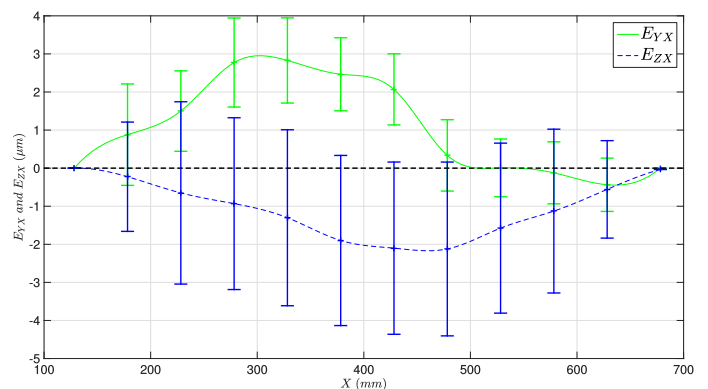


Figure 16. Horizontal and vertical straightness of X-axis: E_{YX} and E_{ZX}

The horizontal and vertical apparent straightness errors are evaluated to less than fifth of the maximal linear positioning error value. Thus, the identified maximum horizontal and vertical apparent straightness errors (E_{YX} and E_{ZX}) are $3 \mu\text{m}$ and $2 \mu\text{m}$ respectively. The angular errors (E_{AX} , E_{BX} and E_{CX}) were also evaluated and the results obtained reveal that E_{BX} reaches a maximum value of $98 \mu\text{m}/\text{m}$. Nevertheless, E_{AX} and E_{CX} present smaller values inferior to $10 \mu\text{m}/\text{m}$ and $40 \mu\text{m}/\text{m}$ respectively.

The combination of apparent linear positioning, apparent straightness and angular errors together can significantly increase the translational error motions in the workspace.

In addition, an error bar is associated to each point of interest.

The error bars are calculated when applying the propagation of the aforementioned uncertainty components. Despite, the equations 10, 11, 12 are linear, the calculation of points of interests is based on the least squares algorithms which are not linear.

As a consequence, the uncertainty propagation is computed using the Monte Carlo method [40], with 10^3 iterations. This strategy is adopted here since the reproductibility of measurement is taken into account, in particular, using the Gaussian (normal) distribution for each probed point along the patterns. The selection of the Gaussian distribution was deduced when analyzing the reproductibility of each measured point, based on the calculated mean and standard deviation values. Furthermore, due to the guideways are manufactured, grinded and

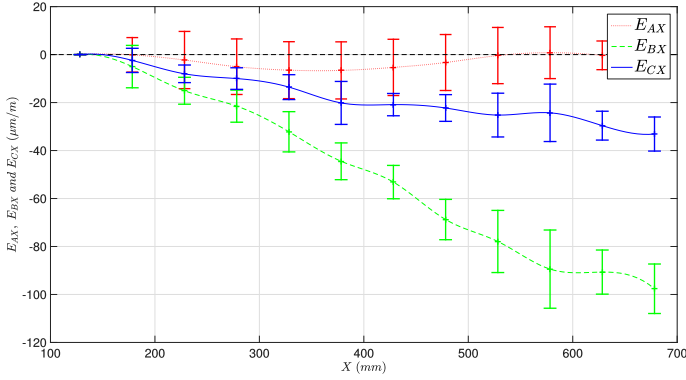


Figure 17. Roll, pitch and yaw of X-axis: E_{AX} , E_{BX} and E_{CX}

honed, the motion errors are continuous in tangency and in curvature. Therefore the data illustrated in figures 15, 16 and 17 are interpolated by a spline interpolation model of class C^2 , leading to provide potential accurate compensation models for E_{XX} , E_{YX} , E_{ZX} , E_{AX} , E_{BX} and E_{CX} .

Thanks to the calibration of the MT using the developed traceable thermo-invariant MFB to the SI metre defined at BIPM and realised at LNE (primary standard (Femtosecond laser)), its metrology traceability becomes also linked to the international traceability chain as illustrated in figure 18.

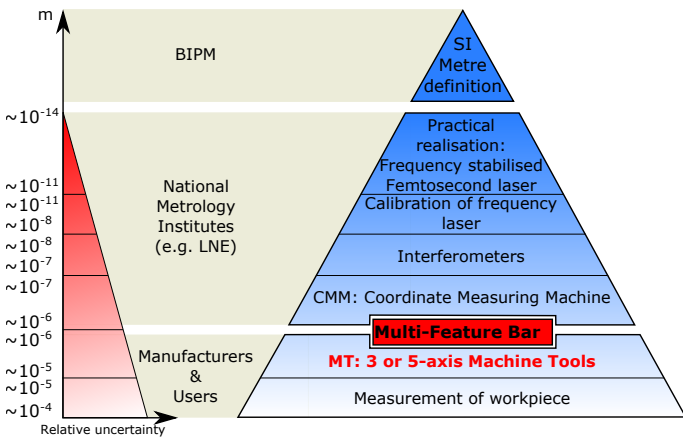


Figure 18. Integration of MFB in traceability chain to the SI metre definition

7. Conclusion

In this study, a Multi-Feature bar (MFB) made of thermo-invariant material (Invar) was defined and developed to calibrate MTs. The design of the MFB involves several patterns, including cylindrical and planar geometric entities, useful to extract 12 points of interests and then providing 3 geometric errors (linear positioning error and 2 straightnesses) for only one position of the MFB. For each position or orientation of the MFB, 316 measured points are necessary for the extraction of the 12 points of interests. Afterwards, the developed MFB was

carefully calibrated on an accurate CMM traceable to the SI meter definition at LNE. The calibration of the MFB was carried out when applying the reversal technique in order to separate the motion errors of the CMM and the true intrinsic parameters of the MFB. This strategy provides a high accurate calibration of the MFB. One main advantage of the MFB model developed is that it can be used directly under harsh environment. Once the MFB was calibrated, it was used for the calibration of the Mikron UCP710 MT to show the efficiency of the standard and proposed method. The calibration of the 3 linear axes of the investigated MT enables the identification of the well known 21 geometric errors of the developed model. For this purpose, the number of positions was optimized using both rotary axes to decrease the required positions of the MFB from 14 to only 6. Further works will be conducted in order to compare the obtained results (Mikron geometric errors) with those obtained with an accurate Laser Tracer. An additional inter-comparison between several NMIs (National Metrology Institutes) will be conducted on the MFB calibration within the EMRP IND62: JRP-TIM project.

8. Acknowledgement

This work was funded through the European Metrology Research Programme (EMRP) Project IND62: JRP-TIM (Traceable In-process dimensional Measurement). The authors sincerely thank the EMRP organization. The EMRP is jointly funded by the EMRP participating countries within EURAMET and the European Union (IND62: JRP-TIM).

Appendix A. Least squares algorithm for cylinder

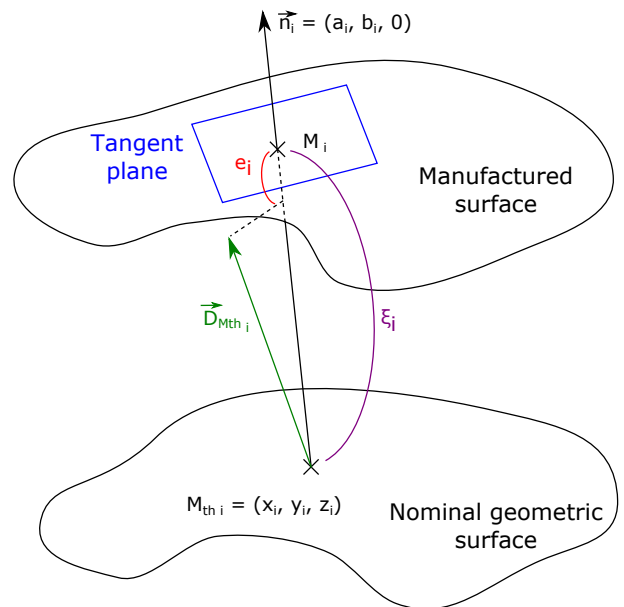


Figure A.19. General geometric identification method of surface [41]

The least squares method is applied on measured data in order to extract the nominal Z-axis cylinder. The points $M_{th(i)}$

are obtained after translation and rotation of measured cloud of points to define the nominal geometry of the cylinder directly centered on the machine frame R_f .

By applying the principle and the description of the small displacement screw (SDS) method (Figure A.19) described in [35] to evaluate the cylindricity, for the spatial coordinates of the point $M_{thi} = (x_i, y_i, z_i)$, the normal vector \vec{n}_i , the variation in measurement parameters ξ_i , the Plücker coordinates screw $[P_i]_A$ and the SDS $[T_A]$ are respectively defined in equations A.1, A.2, A.3 and A.4:

$$\vec{n}_i = \begin{pmatrix} \cos\theta_i = \frac{x_i}{\sqrt{x_i^2 + y_i^2}} \\ \sin\theta_i = \frac{y_i}{\sqrt{x_i^2 + y_i^2}} \\ 0 \end{pmatrix} \quad (A.1)$$

with θ_i being the angular position step.

$$\xi_i = \sqrt{x_i^2 + y_i^2} - R \quad (A.2)$$

$$[P_i]_A = \begin{Bmatrix} \cos\theta_i & -z_i \times \sin\theta_i \\ \sin\theta_i & z_i \times \cos\theta_i \\ 0 & 0 \end{Bmatrix} \quad (A.3)$$

$$[T_A] = \begin{Bmatrix} \alpha & u \\ \beta & v \\ 0 & 0 \end{Bmatrix} \quad (A.4)$$

To obtain the least squares cylinder fitting as close as possible to the measured cloud of points, the problem minimizing the deviation e_i presented in equation A.5 should be solved.

$$e_i = \xi_i - (-z_i \sin\theta_i \alpha + z_i \cos\theta_i \beta + \cos\theta_i u + \sin\theta_i v + r) \quad (A.5)$$

where r is the radius increase along \vec{n}_i that minimizes the variation e_i .

To minimize the sum of square deviations W in equation A.6, it amounts to solve the system of equations A.7. This system can be written using matrix formula A.8 and computation enables the obtained values of parameters (α, β, u, v, r) .

$$W = \sum_{i=1}^n e_i^2 \quad (A.6)$$

where n is the number of measured points

$$\frac{\partial W}{\partial \alpha} = 0; \quad \frac{\partial W}{\partial \beta} = 0; \quad \frac{\partial W}{\partial u} = 0; \quad \frac{\partial W}{\partial v} = 0; \quad \frac{\partial W}{\partial r} = 0 \quad (A.7)$$

$$\begin{bmatrix} \Sigma z_i^2 \sin^2 \theta_i & -\Sigma z_i^2 \sin \theta_i \cos \theta_i & -\Sigma z_i \sin \theta_i \cos \theta_i & -\Sigma z_i \sin^2 \theta_i & -\Sigma z_i \sin \theta_i \\ -\Sigma z_i^2 \sin \theta_i \cos \theta_i & \Sigma z_i^2 \cos^2 \theta_i & \Sigma z_i \cos^2 \theta_i & \Sigma z_i \sin \theta_i \cos \theta_i & \Sigma z_i \cos \theta_i \\ -\Sigma z_i \sin \theta_i \cos \theta_i & \Sigma z_i \cos^2 \theta_i & \Sigma \cos^2 \theta_i & \Sigma \sin \theta_i \cos \theta_i & \Sigma \cos \theta_i \\ \Sigma z_i \sin^2 \theta_i & \Sigma z_i \sin \theta_i \cos \theta_i & \Sigma \sin \theta_i \cos \theta_i & \Sigma \sin^2 \theta_i & \Sigma \sin \theta_i \\ -\Sigma z_i \sin \theta_i & \Sigma z_i \cos \theta_i & \Sigma \cos \theta_i & \Sigma \sin \theta_i & n \end{bmatrix} \times \begin{bmatrix} \alpha \\ \beta \\ u \\ v \\ r \end{bmatrix} = \begin{bmatrix} -\Sigma \xi_i z_i \sin \theta_i \\ \Sigma \xi_i z_i \cos \theta_i \\ \Sigma \xi_i \cos \theta_i \\ \Sigma \xi_i \sin \theta_i \\ \Sigma \xi_i \end{bmatrix} \quad (A.8)$$

The flowchart of the least squares cylinder algorithm is shown in figure A.20. The algorithm outputs are the sum of square deviations, and intrinsic parameters of cylinder: the normal vector, a point of the axis and the radius.

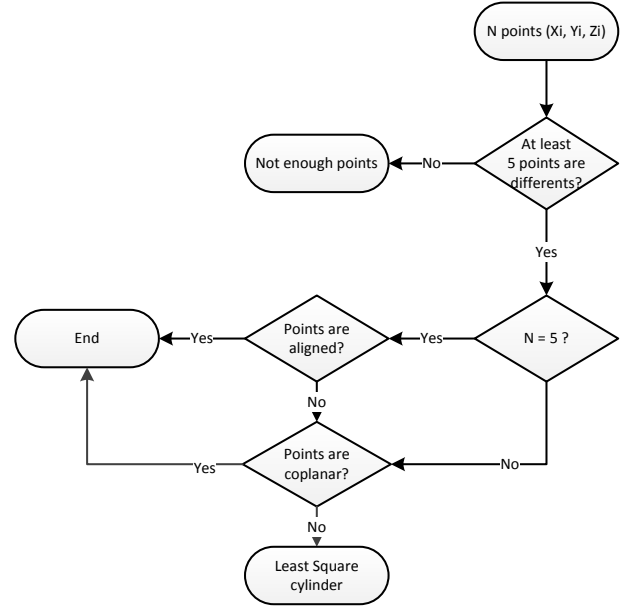


Figure A.20. Flowchart of least squares cylinder algorithm

Appendix B. Least squares algorithm for plane

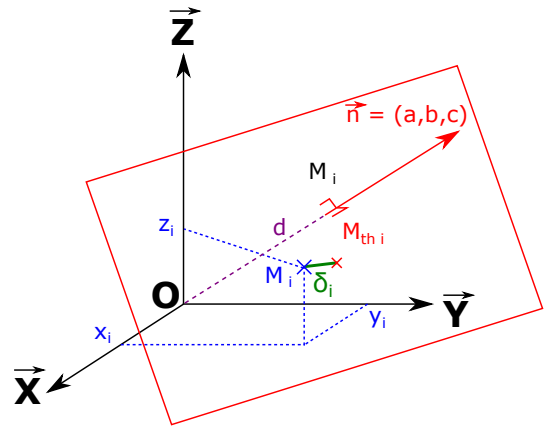


Figure B.21. Description of deviation δ_i

The general form of the equation of plane is:

$$ax + by + cz + d = 0 \quad (B.1)$$

where the normal vector of plane is $\vec{n} = (a, b, c)$ and d is the distance to the frame origin and $M_{thi} = (x, y, z)$ a point of the plane. The following description does not explain particular cases when the distance between the plane and frame origin is equal to zero and when the plane is parallel to \vec{Z} (i.e. $c =$

0). However, the developed algorithm takes into account these cases.

The least squares plane passes as close as possible to the measured cloud of points $M_i = (X_i, Y_i, Z_i)$ by minimizing the sum of square deviations. This square deviation presented in equation B.2 and shown in figure B.21 is obtained from B.1 by applying the variable change defined in equation B.3.

$$\delta_i^2 = \frac{1}{A^2+B^2+1}(AX_i + BY_i + Z_i - D)^2 \quad (B.2)$$

with

$$A = a/c; B = b/c; D = -d/c \quad (B.3)$$

So, for a cloud of n points $M_i = (X_i, Y_i, Z_i)$, the sum W of square deviations δ_i is given by:

$$W = \sum_{i=1}^n \delta_i^2 = \frac{1}{A^2 + B^2 + 1} \sum_{i=1}^n (AX_i + BY_i + Z_i - D)^2 \quad (B.4)$$

the minimum of this sum is obtained when the partial derivatives with respect to A, B and D are equal to zero. The partial derivative with respect to D is particularly simple:

$$\frac{\partial W}{\partial D} = \frac{2}{A^2 + B^2 + 1} \sum_{i=1}^n (AX_i + BY_i + Z_i - D) = 0 \quad (B.5)$$

So the best estimate of D is equal to:

$$D = \frac{1}{n} \left(A \sum_{i=1}^n X_i + B \sum_{i=1}^n Y_i + \sum_{i=1}^n Z_i \right) \quad (B.6)$$

By using the following change of variables:

$$x_i = X_i - \frac{1}{n} \sum_{i=1}^n X_i; \quad y_i = Y_i - \frac{1}{n} \sum_{i=1}^n Y_i; \quad z_i = Z_i - \frac{1}{n} \sum_{i=1}^n Z_i$$

the sum W of square deviations δ_i (equation B.4) can be written as follows:

$$W = \sum_{i=1}^n \delta_i^2 = \frac{1}{A^2 + B^2 + 1} \sum_{i=1}^n (Ax_i + Bx_i + z_i)^2 \quad (B.7)$$

The aim of this method is to perform least squares plane by non iterative method. The mathematical problem is based on the minimization of the sum of square deviations presented in equation B.7. The system of two equations with two unknowns (A, B) is obtained by the partial derivations. This system can be analytically simplified by a polynomial function with degree 3 in A and an expression of B which depends of A. For a polynomial with degree 3 (equation B.8), the coefficient c_0, c_1, c_2 and c_3 can be formulated as follows:

$$c_3A^3 + c_2A^2 + c_1A + c_0 = 0 \quad (B.8)$$

where,

$$\begin{cases} c_3 = S_{xy}(S_{yz}^2 - S_{xz}^2) + S_{xz}S_{yz}(S_{xx} - S_{yy}) \\ c_2 = S_{yz}^3 + S_{yz}(S_{xz}^2 - 2S_{xy}^2 - S_{xx}^2) \\ \quad + S_{yz}(S_{xx}S_{zz} + S_{xx}S_{yy} - S_{yy}S_{zz}) \\ \quad + S_{xy}S_{xz}(S_{xx} + S_{yy} - 2S_{zz}) \\ c_1 = S_{xy}^3 + S_{xy}(S_{xz}^2 - 2 * S_{yz}^2 - S_{zz}^2) \\ \quad + S_{xy}(S_{xx}S_{zz} + S_{yy}S_{zz} - S_{xx}S_{yy}) \\ \quad + S_{xz}S_{yz}(S_{yy} + S_{zz} - 2S_{xx}) \\ c_0 = S_{yz}(S_{xy}^2 - S_{xz}^2) + S_{xy}S_{xz}(S_{zz} - S_{yy}) \end{cases}$$

with,

$$\begin{aligned} S_{xx} &= \sum_{i=1}^n x_i^2 & S_{yy} &= \sum_{i=1}^n y_i^2 & S_{zz} &= \sum_{i=1}^n z_i^2 \\ S_{xy} &= \sum_{i=1}^n x_i y_i & S_{xz} &= \sum_{i=1}^n x_i z_i & S_{yz} &= \sum_{i=1}^n y_i z_i \end{aligned}$$

The expression of B is defined by:

$$B = \frac{S_{xy}S_{yz}A^2 + (S_{yz}^2 - S_{xy}^2)A - S_{xy}S_{yz}}{(S_{yz}(S_{xx} - S_{yy}) - S_{xy}S_{xz})A + S_{xy}(S_{yy} - S_{zz}) + S_{xz}S_{yz}} \quad (B.9)$$

Among the applicable solutions, the logical choice is the ordered pair (A, B) which minimizes W in equation B.4.

The global flowchart of the mathematical algorithm is depicted in figure B.22. The algorithm outputs are intrinsic parameters of plane (i.e. the normal vector, a distance from origin of frame and the plane), and the sum of square deviations. Afterwards, the intrinsic parameters of the least squares plane are deduced by:

$$a = \frac{A}{\sqrt{A^2 + B^2 + 1}}; \quad b = \frac{B}{\sqrt{A^2 + B^2 + 1}}; \quad c = \frac{1}{\sqrt{A^2 + B^2 + 1}}$$

$$d = -\frac{1}{n\sqrt{A^2 + B^2 + 1}} \left(A \sum_{i=1}^n X_i + B \sum_{i=1}^n Y_i + \sum_{i=1}^n Z_i \right)$$

References

- [1] JCGM 200, International vocabulary of metrology basic and general concepts and associated terms (VIM) - 3rd edition (2012).
- [2] IBSPE, IBS Precision Engineering. URL <http://www.ibspe.com>
- [3] R. Ramesh, M. Mannan, A. Poo, Error compensation in machine tools a review: Part i: geometric, cutting-force induced and fixture-dependent errors, International Journal of Machine Tools and Manufacture 40 (9) (2000) 1235 – 1256. doi:[http://dx.doi.org/10.1016/S0890-6955\(00\)00009-2](http://dx.doi.org/10.1016/S0890-6955(00)00009-2). URL <http://www.sciencedirect.com/science/article/pii/S0890695500000092>
- [4] ISO 230-1, Test code for machine tools – part 1: Geometric accuracy of machines operating under no-load or quasi-static conditions (2012).
- [5] ISO 230-7, Test code for machine tools – part 7: Geometric accuracy of axes of rotation (2007).

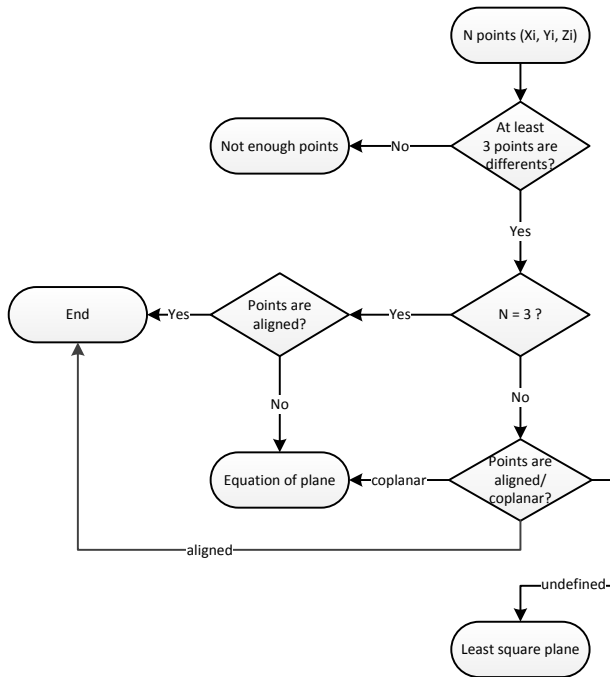


Figure B.22. Flowchart of least squares plane algorithm

- [6] P. Cauchick-Miguel, T. Kinga, J. Davis, {CMM} verification: a survey, *Measurement* 17 (1) (1996) 1 – 16. doi:[http://dx.doi.org/10.1016/0263-2241\(96\)00001-2](http://dx.doi.org/10.1016/0263-2241(96)00001-2). URL <http://www.sciencedirect.com/science/article/pii/S0263224196000012>
- [7] W. Knapp, U. Tschudi, A. Bucher, Comparison of different artefacts for interim coordinate-measuring machine checking: a report from the swiss standards committee, *Precision Engineering* 13 (4) (1991) 277 – 291. doi:[http://dx.doi.org/10.1016/0141-6359\(91\)90006-5](http://dx.doi.org/10.1016/0141-6359(91)90006-5). URL <http://www.sciencedirect.com/science/article/pii/S0141635991900065>
- [8] ISO 10360-2, Geometrical product specifications (gps) – acceptance and reverification tests for coordinate measuring machines (cmm) – part 2: Cmms used for measuring linear dimensions (January 2009).
- [9] S. Osawa, K. Busch, M. Franke, H. Schwenke, Multiple orientation technique for the calibration of cylindrical workpieces on {CMMs}, *Precision Engineering* 29 (1) (2005) 56 – 64. doi:<http://dx.doi.org/10.1016/j.precisioneng.2004.04.006>. URL <http://www.sciencedirect.com/science/article/pii/S014163590400087X>
- [10] K. Busch, H. Kunzmann, F. Wldele, Calibration of coordinate measuring machines, *Precision Engineering* 7 (3) (1985) 139 – 144. doi:[http://dx.doi.org/10.1016/0141-6359\(85\)90036-4](http://dx.doi.org/10.1016/0141-6359(85)90036-4). URL <http://www.sciencedirect.com/science/article/pii/S0141635985900364>
- [11] H. Pahk, J. Kim, Development of computer integrated system for error diagnosis of a cmm using calibrated mechanical artefacts, *International Journal of Machine Tools and Manufacture* 33 (6) (1993) 773 – 790. doi:[http://dx.doi.org/10.1016/0890-6955\(93\)90037-U](http://dx.doi.org/10.1016/0890-6955(93)90037-U). URL <http://www.sciencedirect.com/science/article/pii/S089069559390037U>
- [12] J. Bryan, A simple method for testing measuring machines and machine tools part 1: Principles and applications, *Precision Engineering* 4 (2) (1982) 61 – 69. doi:[http://dx.doi.org/10.1016/0141-6359\(82\)90018-6](http://dx.doi.org/10.1016/0141-6359(82)90018-6). URL <http://www.sciencedirect.com/science/article/pii/S0141635982900186>
- [13] ANSI/ASME, B89.4.1-1997 methods for performance evaluation of coordinate measuring machines (1997).
- [14] Y. Abbaszadeh-Mir, J. R. R. Mayer, G. Cloutier, C. Fortin, Theory and simulation for the identification of the link geometric errors for a five-axis machine tool using a telescoping magnetic ball-bar, *International Journal of Production Research* 40 (18) (2002) 4781–4797. arXiv:<http://www.tandfonline.com/doi/pdf/10.1080/00207540210164459>, doi:10.1080/00207540210164459. URL <http://www.tandfonline.com/doi/abs/10.1080/00207540210164459>
- [15] F. Jouy, A. Clément, Theoretical modelisation and experimental identification of the geometrical parameters of coordinate-machines by measuring a multi-directed bar, {CIRP} Annals - Manufacturing Technology 35 (1) (1986) 393 – 396. doi:[http://dx.doi.org/10.1016/S0007-8506\(07\)61913-1](http://dx.doi.org/10.1016/S0007-8506(07)61913-1). URL <http://www.sciencedirect.com/science/article/pii/S0007850607619131>
- [16] G. Zhang, Y. Zang, A method for machine geometry calibration using 1-d ball array, {CIRP} Annals - Manufacturing Technology 40 (1) (1991) 519 – 522. doi:[http://dx.doi.org/10.1016/S0007-8506\(07\)62044-7](http://dx.doi.org/10.1016/S0007-8506(07)62044-7). URL <http://www.sciencedirect.com/science/article/pii/S0007850607620447>
- [17] J. Ouyang, I. Jawahir, Ball array calibration on a coordinate measuring machine using a gage block, *Measurement* 16 (4) (1995) 219 – 229. doi:[http://dx.doi.org/10.1016/0263-2241\(95\)00035-6](http://dx.doi.org/10.1016/0263-2241(95)00035-6). URL <http://www.sciencedirect.com/science/article/pii/S0263224195000356>
- [18] C. K. Lim, M. Burdekin, Rapid volumetric calibration of coordinate measuring machines using a hole bar artefact, *Proceedings of the Institution of Mechanical Engineers, Part B: Journal of Engineering Manufacture* 216 (8) (2002) 1083–1093. arXiv:<http://pib.sagepub.com/content/216/8/1083.full.pdf+html>, doi:10.1243/095440502760272368. URL <http://pib.sagepub.com/content/216/8/1083.abstract>
- [19] G. Peggs, P. McKeown, Creating a standards infrastructure for co-ordinate measurement technology in the {UK}, {CIRP} Annals - Manufacturing Technology 38 (1) (1989) 521 – 523. doi:[http://dx.doi.org/10.1016/S0007-8506\(07\)62759-0](http://dx.doi.org/10.1016/S0007-8506(07)62759-0). URL <http://www.sciencedirect.com/science/article/pii/S0007850607627590>
- [20] H. Kunzmann, E. Trapet, F. Wldele, A uniform concept for calibration, acceptance test, and periodic inspection of coordinate measuring machines using reference objects, {CIRP} Annals - Manufacturing Technology 39 (1) (1990) 561 – 564. doi:[http://dx.doi.org/10.1016/S0007-8506\(07\)61119-6](http://dx.doi.org/10.1016/S0007-8506(07)61119-6). URL <http://www.sciencedirect.com/science/article/pii/S0007850607611196>
- [21] E. Trapet, F. Wldele, A reference object based method to determine the parametric error components of coordinate measuring machines and machine tools, *Measurement* 9 (1) (1991) 17 – 22. doi:[http://dx.doi.org/10.1016/0263-2241\(91\)90022-I](http://dx.doi.org/10.1016/0263-2241(91)90022-I). URL <http://www.sciencedirect.com/science/article/pii/S026322419190022I>
- [22] T. Liebrich, B. Bringmann, W. Knapp, Calibration of a 3D-ball plate, *Precision Engineering* 33 (1) (2009) 1 – 6. doi:<http://dx.doi.org/10.1016/j.precisioneng.2008.02.003>. URL <http://www.sciencedirect.com/science/article/pii/S0141635908000342>
- [23] B. Bringmann, W. Knapp, Machine tool calibration: Geometric test uncertainty depends on machine tool performance, *Precision Engineering* 33 (4) (2009) 524 – 529. doi:<http://dx.doi.org/10.1016/j.precisioneng.2009.02.002>. URL <http://www.sciencedirect.com/science/article/pii/S014163590900035X>
- [24] B. Acko, M. McCarthy, F. Haertig, B. Buchmeister, Standards for testing freeform measurement capability of optical and tactile coordinate measuring machines, *Measurement Science and Technology* 23 (9) (2012) 094013. URL <http://stacks.iop.org/0957-0233/23/i=9/a=094013>
- [25] J. B. de Aquino Silva, M. Burdekin, A modular space frame for assessing the performance of co-ordinate measuring machines (cmms), *Precision Engineering* 26 (1) (2002) 37 – 48.

- doi:[http://dx.doi.org/10.1016/S0141-6359\(01\)00096-4](http://dx.doi.org/10.1016/S0141-6359(01)00096-4).
URL <http://www.sciencedirect.com/science/article/pii/S0141635901000964>
- [26] J. Choi, B. Min, S. Lee, Reduction of machining errors of a three-axis machine tool by on-machine measurement and error compensation system, *Journal of Materials Processing Technology* 155156 (0) (2004) 2056 – 2064. doi:<http://dx.doi.org/10.1016/j.jmatprot.2004.04.402>.
URL <http://www.sciencedirect.com/science/article/pii/S0924013604005060>
- [27] J. Mayer, Five-axis machine tool calibration by probing a scale enriched reconfigurable uncalibrated master balls artefact, {CIRP} Annals - Manufacturing Technology 61 (1) (2012) 515 – 518. doi:<http://dx.doi.org/10.1016/j.cirp.2012.03.022>.
URL <http://www.sciencedirect.com/science/article/pii/S0007850612000248>
- [28] S. Ibaraki, Y. Ota, A machining test to calibrate rotary axis error motions of five-axis machine tools and its application to thermal deformation test, *International Journal of Machine Tools and Manufacture* 86 (0) (2014) 81 – 88. doi:<http://dx.doi.org/10.1016/j.ijmactools.2014.07.005>.
URL <http://www.sciencedirect.com/science/article/pii/S0890695514000996>
- [29] M. Pezeshki, B. Arezoo, Kinematic errors identification of three-axis machine tools based on machined work pieces, *Precision Engineering* (2015) –doi:<http://dx.doi.org/10.1016/j.precisioneng.2015.09.018>.
URL <http://www.sciencedirect.com/science/article/pii/S0141635915001798>
- [30] H. Castro, M. Burdekin, Dynamic calibration of the positioning accuracy of machine tools and coordinate measuring machines using a laser interferometer, *International Journal of Machine Tools and Manufacture* 43 (9) (2003) 947 – 954. doi:[http://dx.doi.org/10.1016/S0890-6955\(03\)00083-X](http://dx.doi.org/10.1016/S0890-6955(03)00083-X).
URL <http://www.sciencedirect.com/science/article/pii/S089069550300083X>
- [31] H. Schwenke, M. Franke, J. Hannaford, H. Kunzmann, Error mapping of {CMMs} and machine tools by a single tracking interferometer, {CIRP} Annals - Manufacturing Technology 54 (1) (2005) 475 – 478. doi:[http://dx.doi.org/10.1016/S0007-8506\(07\)60148-6](http://dx.doi.org/10.1016/S0007-8506(07)60148-6).
URL <http://www.sciencedirect.com/science/article/pii/S0007850607601486>
- [32] S. Aguado, J. Santolaria, D. Samper, J. Aguilar, Influence of measurement noise and laser arrangement on measurement uncertainty of laser tracker multilateration in machine tool volumetric verification, *Precision Engineering* 37 (4) (2013) 929 – 943. doi:<http://dx.doi.org/10.1016/j.precisioneng.2013.03.006>.
URL <https://www-sciencedirect-com.bibliopam.ens-cachan.fr/science/article/pii/S0141635913000561>
- [33] K. P. Birch, M. J. Downs, An updated edln equation for the refractive index of air, *Metrologia* 30 (3) (1993) 155.
URL <http://stacks.iop.org/0026-1394/30/i=3/a=004>
- [34] ISO 5459, Geometrical product specifications (GPS) – geometrical tolerancing – datums and datum systems (2011).
URL http://www.iso.org/iso/home/store/catalogue_tc/catalogue_detail.htm?csnumber=40358
- [35] H. Noura, P. Bourdet, Evaluation of roundness error using a new method based on a small displacement screw, *Measurement Science and Technology* 25 (4) (2014) 044012.
URL <http://stacks.iop.org/0957-0233/25/i=4/a=044012>
- [36] NF E 11 019, Geometrical product specification (gps) - specific standards - rules of design and characteristics (December 2002).
- [37] C. J. Evans, R. J. Hocken, W. T. Estler, Self-calibration: Reversal, redundancy, error separation, and absolute testing, {CIRP} Annals - Manufacturing Technology 45 (2) (1996) 617 – 634. doi:[http://dx.doi.org/10.1016/S0007-8506\(07\)60515-0](http://dx.doi.org/10.1016/S0007-8506(07)60515-0).
URL <http://www.sciencedirect.com/science/article/pii/S0007850607605150>
- [38] NF ISO 841, Industrial automation systems and integration – numerical control of machines – coordinate system and motion nomenclature (Septembre 2004).
- [39] ISO 10791-6, Test conditions for machining centres – part 6: Accuracy of speeds and interpolations (December 2014).
- [40] JCGM 101, Evaluation of measurement data - Supplement 1 to the "Guide to the expression of the uncertainty in measurement" - Propagation of distributions using a Monte Carlo method (2008).
- [41] Bourdet, Contribution à la Mesure Tridimensionnelle : Modèle d'identification géométrique des surfaces, Métrologie fonctionnelle des pièces mécaniques, Correction géométrique des machines à mesurer tridimensionnelles, Doctorat d'état Es-Sciences Physiques, Univ. NANCY 1 (1987).
URL http://webserv.lurpa.ens-cachan.fr/~bourdet/doc_Theses/These_P-Bourdet.pdf